Materials Advances

ROYAL SOCIETY OF CHEMISTRY

COMMUNICATION

View Article Online
View Journal | View Issue

Check for updates

Cite this: *Mater. Adv.*, 2020, 1, 14

Received 21st February 2020,
Accepted 28th March 2020

DOI: 10.1039/d0ma00045k

rsc.li/materials-advances

3D printing of anisotropic polymer nanocomposites with aligned $BaTiO_3$ nanowires for enhanced energy density†

Hang Luo,[a] Xuefan Zhou,[a] Ru Guo,[a] Xi Yuan,*[a] Hehao Chen,[a] Isaac Abrahams[b] and Dou Zhang*[a]

High power density capacitors possess broad application prospects in electric vehicles and power transmission systems. The development of capacitors with high energy density to realize miniaturization and lightweight application is the bottle-neck in this field. Strategies including orientated distribution of fillers have been utilized to increase the energy density of the dielectrics. In this work, we demonstrate high-performance flexible poly(vinylidene fluoride–chlorotrifluoroethylene) (P(VDF–CTFE)) nanocomposites with aligned $BaTiO_3$ nanowires using 3D printing technology. The 3D printing process is computer-controlled, which can effectively achieve designed geometric shapes and precise size. The resulting $BaTiO_3$ nanowires are highly aligned in a direction parallel to the surface of the nanocomposites due to the high shear environment within the very small 100 μm diameter nozzle. The highest energy density for these nanocomposites, with aligned $BaTiO_3$ nanowires, was 14.52 J cm^{-3}, which is 55% higher than that of nanocomposites with random $BaTiO_3$ nanowires at the same loading level. This facile and readily scalable method of aligning one-dimensional fillers in a polymer matrix has potential not only in dielectric capacitor technology, but also in other fields where directional arrangement of low dimensional nanostructured materials is needed.

1 Introduction

High performance dielectric capacitors have been widely applied in electrical and electronic systems, such as electric vehicles, wind generators and aerospace power conditioning, due to their merits of super high power density and ability to withstand high operating voltage.[1–7] The dielectric materials used in commercially available capacitors are mainly based on biaxially oriented polypropylenes (BOPP), which exhibit energy densities of only 1–1.2 J cm^{-3} at high applied electric field (~640 kV mm^{-1}).[8] In this case, the low energy density of the dielectric becomes a limitation to their applications.[9–11] Generally, the discharge energy density (J_{dis}) of a capacitor is determined by the eqn (1),

$$J_{dis} = \int_0^{D_{max}} E\,dD \quad (1)$$

where D and E are applied electric field and the electric displacement, respectively.[12–14] For linear dielectrics, J_{dis} can be evaluated by eqn (2)

$$J_{dis} = \frac{1}{2}\varepsilon_0\varepsilon_r E^2 \quad (2)$$

where ε_0 is the permittivity of free space and ε_r is the relative permittivity of the dielectrics. Therefore, two key parameters for enhancing J_{dis} are the relative permittivity and the largest applied electric field *i.e.* the breakdown strength (E_b).[15–17] PVDF based nanocomposites with embedded ferroelectric ceramics such as $BaTiO_3$,[18,19] $Ba_{1-x}Sr_xTiO_3$,[20] and $Pb(Zr_{1-x}Ti_x)O_3$[21] show enhanced energy density due to the combination of the high relative permittivity from the ferroelectric ceramics and high breakdown strength from the PVDF polymer matrix. In our previous work, ceramic fillers with high aspect ratios, such as $BaTiO_3$,[22–24] $Na_{0.5}Bi_{0.5}TiO_3$,[25] TiO_2@PZT,[26,27] and $Na_2Ti_3O_7$ nanowires[28] were employed to build dielectric capacitors with improved permittivity and energy density. The improvment in energy density is attributed to the high breakdown strength mainatined by low ceramic loadings and increased relative permittivity due to the high aspect ratio fillers.[29] In ceramic/polymer nanocomposites, electrons can move from one nanowire to another when the nanowires are randomly distributed due to multiple cross contacts between wires. This tunneling effect[30,31] leads to lowering of breakdown strength. In contrast, if the ceramic nanowires are arranged in the polymer matrix in an orientated direction, *e.g.* perpendicular to the electric field, the electronic transmission pathway is blocked resulting in an enhanced breakdown strength.[32] Andrews *et al.* focused on finite element models to

[a] State Key Laboratory of Powder Metallurgy, Central South University, Changsha, Hunan 410083, China. E-mail: dzhang@csu.edu.cn
[b] Materials Research Institute, School of Biological Sciences, Queen Mary University of London, Mile End Road, London E1 4NS, UK

† Electronic supplementary information (ESI) available. See DOI: 10.1039/d0ma00045k

demonstrate that the orientation of the filler plays a critical role in achieving high dielectric and electromechanical coupling in the composites.[33] Exprimental work using different strategies, such as tape-casting,[34] uniaxial strain,[21] and electrospinning[35,36] demonstrated that spatial distribution of the fillers also plays a large role in the dielectric and energy storage properties of the composites. A major obstacle lies in developing an effective technique for aligning the one dimensional fillers in the polymer matrix. Three-dimensional printing (3D printing, also known as additive manufacturing) is widely regarded as a revolution in manufacturing technology, with significant promise for electronic applications.[37–39] During the printing process, the ceramic/polymer slurry experiences a high shear environment within the very small nozzle (typically with a diameter of 100 μm), which will produce high orientation of the fillers and form anisotropic materials.[39,40] In addition, 3D printing is a computer-controlled technique, which can print samples with designed geometric shape, precise size, short processing times and at low cost.[41,42] Here, we demonstrated high-performance flexible poly(vinylidene fluoride–chlorotrifluoroethylene) (P(VDF–CTFE)) nanocomposites with aligned $BaTiO_3$ nanowires using 3D printing technology. $BaTiO_3$ nanowires were embedded and aligned in a P(VDF–CTFE) polymer matrix by tunable internal friction during the extrusion. The rheological properties of the $BaTiO_3$/P(VDF–CTFE) slurry with $BaTiO_3$ loadings that lead to the orientation during the 3D printing process were investigated. Significant performance enhancements, including breakdown strength and energy density improvements, were achieved compared with nanocomposites prepared by a casting method. We believe that 3D printing technology has great potential in the development of dielectric nanocomposites with controllable anisotropic properties for a broad range of applications.

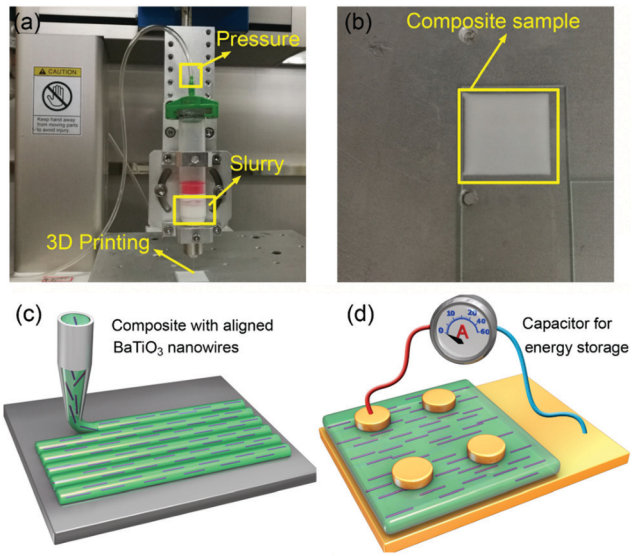

Fig. 1 Alignment of $BaTiO_3$ nanowires in nanocomposites: photographs of (a) the printing assembly and (b) a printed nanocomposite sample; schematic illustrations of (c) the alignment of $BaTiO_3$ nanowires in the P(VDF–CTFE) matrix and (d) a nanocomposite capacitor for energy storage applications.

2 Experimental

2.1 Synthesis of $BaTiO_3$ nanowires

The main materials used in the experiments are purchased from Sinopharm chemical reagent Co. Ltd., China, including titanium oxide powders (TiO_2, anatase, 99.9% purity), sodium hydroxide (NaOH, 96% purity), Barium hydroxide octahydrate ($Ba(OH)_2{\cdot}8H_2O$, 99.9% purity), hydrochloric acid solution (HCl, 37 wt%), and dimethylformamide solvent (DMF, 99.5% purity). The P(VDF–CTFE) powders with 15% CTFE are provided by PolyK Technologies, LLC, USA. All other chemicals were used "as received," except for special notes. The $BaTiO_3$ nanowires were synthesized by a hydrothermal method according to previous work.[43] Firstly, 1.446 g of TiO_2 was added to 70 ml NaOH solution (10 M) and the mixture was stirred for 2 h to form a homogeneous suspension. The hydrothermal reactions were carried out at 210 °C under an auto-generated pressure for 24 h in a 100 ml Teflon-lined autoclave. The $Na_2Ti_3O_7$ products were washed using distilled water and then soaked in diluted 0.2 M HCl solution for 4 h to obtain hydrogen titanate nanowires ($H_2Ti_3O_7$). Secondly, 0.150 g $H_2Ti_3O_7$ were dispersed in 70 ml $Ba(OH)_2{\cdot}8H_2O$ solution (0.1 M) and the mixture was sonicated for 10 min. The hydrothermal reactions were carried out at 210 °C under auto-generated pressure for 24 h in a 100 ml Teflon-lined autoclave. The products were soaked in 0.2 M HCl solution briefly, then washed with distilled water several times and dried at 80 °C in an oven.

2.2 Fabrication of $BaTiO_3$/P(VDF–CTFE) dielectric nanocomposites

The anisotropic nanocomposites were fabricated using a deposition device based on a dispersing system (DR2203, EFD Inc., East Province, RI) according to our previous work.[44] 8 g of P(VDF–CTFE) was dissolved in 92 g dimethylformamide (DMF) and then was concentrated by evaporating the solvent to obtain high viscosity for printing. Samples with volume fractions of 2.5, 5.0 and 7.5% $BaTiO_3$ nanowires relative to the P(VDF–CTFE) were prepared. Fig. 1a and b show optical photographs of the 3D printing equipment and a printed sample. The P(VDF–CTFE)/$BaTiO_3$/DMF mixtures were stirred and ultrasonically treated to form a uniform slurry. The slurry was transferred to an extrusion syringe with a nozzle of 100 μm diameter and pressure of 10–20 psi. All of the samples were printed at room temperature on a three-axis CNC platform controlled by a computer regulator. The composites with randomly distributed $BaTiO_3$ nanowires were prepared by a casting method. $BaTiO_3$ nanowires were dispersed in 70 : 30 (volume fraction) acetone/DMF hybrid solvent with sonication and stirring, and then mixed with P(VDF–CTFE) powder for further stirring and sonication for 48 h. The suspension was cast onto the surface of a clean glass, and dried at 80 °C for 12 h at vacuum. The capacitors were prepared by sputtering the Au electrode with a diameter of 2 mm using metal mask.

2.3 Characterization

The crystalline phases of $BaTiO_3$ nanowires were evaluated by X-ray powder diffraction (XRD, Rigaku D/max 2550, Japan) with

Cu-Kα radiation (λ = 1.5418 Å) at room temperature. The morphology of the $BaTiO_3$ nanowires and nanocomposite films were observed using a scanning electron microscope (SEM, Nova NanoSEM230, USA). High-resolution transmission electron microscopy (HR-TEM) images of the $BaTiO_3$ nanowires were taken with a Titan G2 60-300, using an accelerating voltage of 300 kV. The morphology and orientation of the nanowire composites were examined using polarizing microscopy (POM, Leica DM-LM-P). The rheological properties of the $BaTiO_3$/P(VDF–CTFE) slurry were studied using a rotational rheometer (AR2000 EX, TA Instruments, New Castle, DE) with a parallel plate diameter of 40 mm. The frequency dependent permittivity and dielectric loss of the nanocomposite films were measured using an Agilent 4294A LCR meter with frequency ranging from 100 Hz to 10 MHz. The electric displacement–electric field (D–E) loops was measured using a TF analyzer 2000 ferroelectric polarization tester (aixACT, Germany) and Delta 9023 furnace in a silicone oil bath at room temperature and 10 Hz.

3 Results and discussion

Fig. 1c and d show sketches of anisotropic nanocomposites with aligned $BaTiO_3$ nanowires induced by shear stress along the printing direction. During the extrusion process, the $BaTiO_3$ nanowires suffer from a high shear environment along the inner wall of the 100 μm diameter nozzle, which forces the $BaTiO_3$ nanowires to align parallel to the direction of printing.

$BaTiO_3$ nanowires were selected as the fillers due to the advantages of high permittivity and low dielectric loss.[45–48] Firstly, high aspect ratio $Na_2Ti_3O_7$ nanowires with smooth surface were prepared, of which the morphologies and crystal structure were confirmed as shown in Fig. S1a and b (ESI†). Then, the $Na_2Ti_3O_7$ nanowires were converted into $H_2Ti_3O_7$ and finally to $BaTiO_3$ nanowires in the second step of the hydrothermal reaction. It is clear that the $BaTiO_3$ nanowires possess super-high aspect ratios and uniform morphology, as shown in Fig. 2a and Fig. S1c (ESI†). Fig. S1d (ESI†) shows the XRD pattern of $BaTiO_3$ nanowires, which can be attributed to the tetragonal phase of $BaTiO_3$ (PDF: 31-0174). Fig. 2b shows a high resolution transmission electron microscrograph of a single $BaTiO_3$ nanowire. Parallel lattice spacing of approximately 0.36 nm and 0.20 nm, corresponding to the $(1\bar{3}1)$ and (002) planes of the tetragonal phase, respectively were identified. The distribution of $BaTiO_3$ nanowire fillers in the nanocomposites is seen in the SEM and POM images shown Fig. 1c and d, respectively. It is clear that the $BaTiO_3$ nanowires are well dispersed and aligned in one direction in the nanocomposite. For comparison, the SEM and POM images of the nanocomposites with randomly distributed $BaTiO_3$ nanowires prepared by the casting method are shown Fig. S2e, f and S3b (ESI†).

Fig. 3a shows the relationship between shear rate and viscosity in P(VDF–CTFE) slurries with different volume fractions of $BaTiO_3$ nanowires. The slurries show shear thinning characteristics at low shear rate, and when the shear rate increases to around 100 s^{-1}, the viscosity of slurries is close to a constant value.

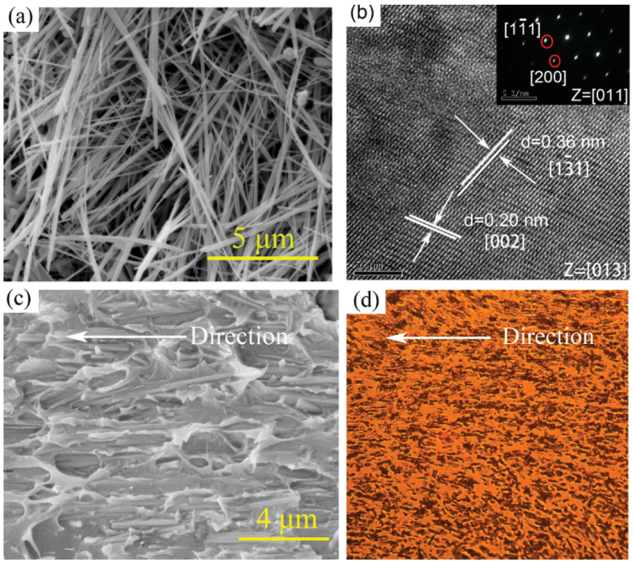

Fig. 2 (a) SEM image of $BaTiO_3$ nanowires; (b) HRTEM image of a single $BaTiO_3$ nanowire; (c) SEM and (d) POM images of nanocomposites prepared by 3D printing with 5 vol% aligned $BaTiO_3$ nanowires.

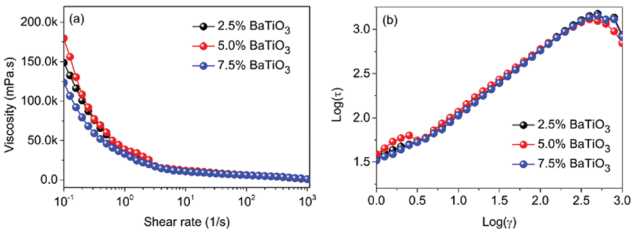

Fig. 3 (a) Shear rate dependence of viscosity and (b) logarithmic plot of shear stress of the slurries with various $BaTiO_3$ loadings.

At the shear rate of 100 s^{-1}, the viscosity of the three samples is about 6.7 mPa s, which means that the change of filler loadings over a very small range shows little effect on the viscosity of the slurry. Fig. 3b shows the shear rate dependent shear stress of slurries with different $BaTiO_3$ nanowires loadings. The slope of the curves represents the viscosity of the suspension. At a constant shear rate, the slurries shows similar viscosity, which is consistent with the results shown in Fig. 3a. Slurries with shear thinning behavior meet the rheological requirements for application in 3D direct writing. At low shear rate, the slurries shows high viscosity, which allow them to avoid agglomeration and settling of the $BaTiO_3$ nanowires within the printing needle tube. At high shear rate, the slurries show low viscosity, which allows them to have sufficient fluidity to be extruded from the printing needle.[49,50]

Nanocomposites with different $BaTiO_3$ nanowire loadings were prepared by the 3D direct writing method and compared with those made using a traditional solution casting method. The permittivity and dielectric loss of the prepared nanocomposites are summarized in Fig. 4. Fig. 4a and c show the frequency dependent permittivity of $BaTiO_3$ nanowire/P(VDF–CTFE) nanocomposites, where the $BaTiO_3$ nanowires are aligned perpendicular to electric field direction (Fig. 4a) compared to the random

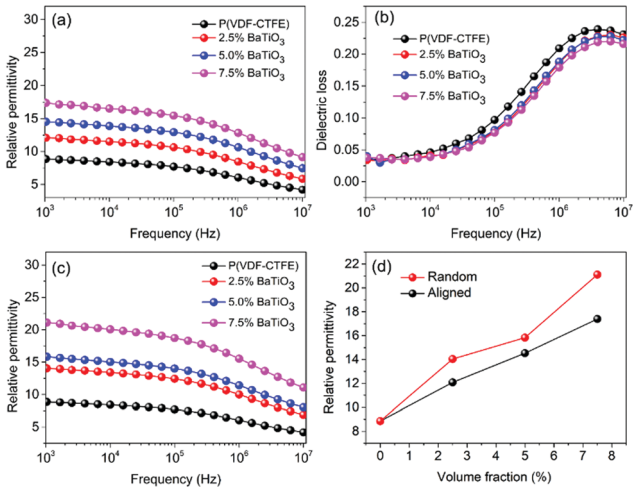

Fig. 4 Frequency dependence of (a) relative dielectric permittivity and (b) dielectric loss of $BaTiO_3$/P(VDF–CTFE) nanocomposites with aligned $BaTiO_3$ nanowires, (c) relative dielectric permittivity of nanocomposites with random distributed $BaTiO_3$ nanowires; (d) relative dielectric permittivity of the nanocomposites as a function of volume fraction at 1 kHz.

distribution (Fig. 4c). The permittivity of the nanocomposites with aligned $BaTiO_3$ nanowires is smaller than that of nanocomposites with random $BaTiO_3$ nanowires. For example, when the loadings of random $BaTiO_3$ nanowires is 2.5, 5.0 and 7.5 vol%, the permittivity of the nanocomposites with random $BaTiO_3$ nanowires is 14, 15.5 and 21.5, respectively, while the permittivity of the nanocomposites with aligned $BaTiO_3$ nanowires is 12, 14 and 17.5, respectively (Fig. 4d).

The total permittivity over the high and low frequency ranges ε' is the sum of interfacial and space charge contributions (eqn (3)):

$$\varepsilon' = \varepsilon_{MWS}' + \varepsilon_{DIP}' \quad (3)$$

where ε_{MWS}' and ε_{DIP}' represent interfacial polarization (in the low frequency range) and space charge polarization (in the high frequency range). Polarization (P) can be calculated using eqn (4):

$$P = \frac{\sum \mu}{V} = \frac{\sum ql}{V} \quad (4)$$

where q, l, and V are charge, distance between positive and negative charges and volume of the sample. When the ceramic fillers are distributed parallel to the electric field direction, l is equal to the length of the ceramic nanowires (~several microns). When the ceramic fillers are distributed perpendicular to the electric field, l is equal to the diameter of the ceramic nanowires (~100 nm). This can explain lower permittivity of nanocomposites with aligned $BaTiO_3$ nanowires compared to that of nanocomposites with randomly distributed $BaTiO_3$ nanowires.[32,36]

Fig. 5a shows typical P–E loops for P(VDF–CTFE) nanocomposites with aligned $BaTiO_3$ nanowires, from which the saturation polarization and residual polarization can be obtained and the energy density can be calculated. Due to the high permittivity of $BaTiO_3$ fillers and the introduction of interfacial polarization, the saturation polarization increases with increasing $BaTiO_3$ loading. When the loading of aligned $BaTiO_3$ nanowires is 2.5 vol%,

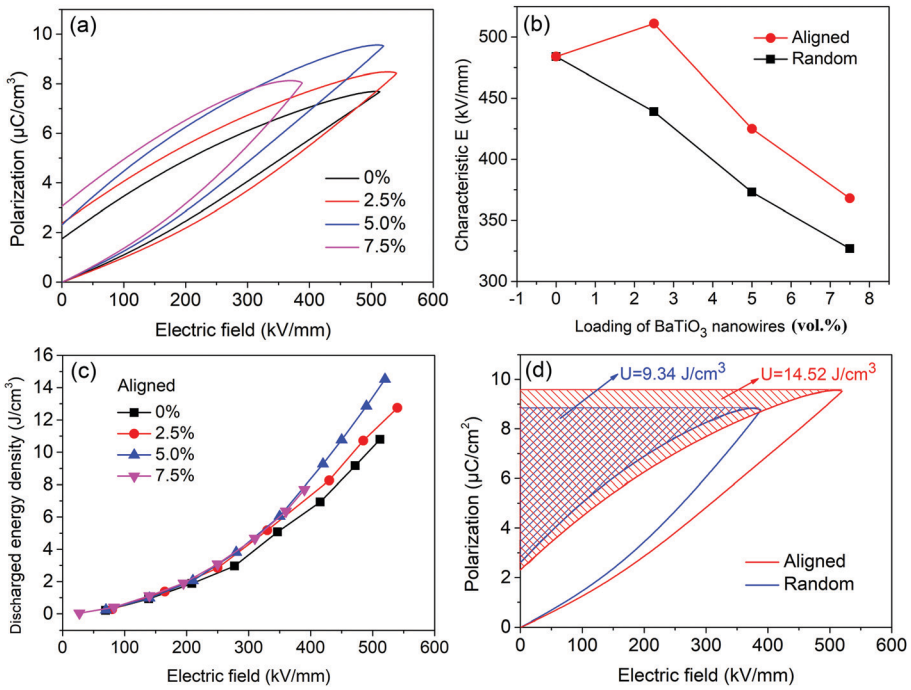

Fig. 5 (a) P–E loops and (c) discharge energy density of P(VDF–CTFE) nanocomposites filled with aligned $BaTiO_3$ nanowires; (b) breakdown strength of P(VDF–CTFE) nanocomposites as a function of $BaTiO_3$ loading; (d) comparison of maximum discharged energy density and P–E loops of P(VDF–CTFE) nanocomposites with 5.0 vol% aligned and randomly distributed $BaTiO_3$ nanowires.

the nanocomposites achieve higher polarization and breakdown strength (Fig. S4, ESI†) than that in P(VDF–CTFE). This means that nanocomposites with low loadings of aligned $BaTiO_3$ nanowires can simultaneous improve permittivity and breakdown strength. Fig. 5b shows the characteristic breakdown strengths of nanocomposites with aligned and random $BaTiO_3$ nanowires at various loading. The nanocomposite with aligned $BaTiO_3$ nanowires possesses higher breakdown strength than the nanocomposite with random $BaTiO_3$ nanowires at the same loading level. The discharged energy density of the nanocomposites with aligned $BaTiO_3$ nanowires as a function of applied electric field is shown in Fig. 5c. The discharged energy density of all composites is similar at low field, but at high field increases with increasing loading level. The maximum energy density achieved in nanocomposites with aligned $BaTiO_3$ nanowires was 14.52 J cm^{-3} for the sample with 5.0 vol% loading, which is 55% higher than that of the nanocomposite with randomly aligned $BaTiO_3$ nanowires at the same loading level. The energy density is directly determined by two factors including the relatively permittivity (polarization) and breakdown strength of the composite according to eqn (2). Incorporated $BaTiO_3$ fillers into the polymer matrix, the permittivity (polarization) of the composite will be increased and which will continue to increase with the loading of $BaTiO_3$ fillers due to the high permittivity of the $BaTiO_3$ itself. However, high loading of $BaTiO_3$ filler will introduce inevitable defects, in addition, the mismatch between the filler and matrix will lead to the concentration of electric field distribution, both of which will decrease the breakdown strength of the composites. It means that the permittivity and breakdown strength are two contradictory factors. The results showed that the composite with 5.0 vol% $BaTiO_3$ nanowires get the balance point, which simultaneously achieved high polarization and breakdown strength.[51,52]

4 Conclusions

It has been shown that 3D printing is an effective method to prepare aligned $BaTiO_3$ nanowires/P(VDF–CTFE) nanocomposites. P(VDF–CTFE) nanocomposites with aligned $BaTiO_3$ nanowires possess higher breakdown strength and energy density compared to those with randomly distributed $BaTiO_3$ nanowires, with a maximum discharged energy density of 14.52 J cm^{-3} achieved with 5.0 vol% nanowire loading, 55.5% higher than that of nanocomposites with randomly distributed nanowires at the same loading level. This work provides a facile route to align one dimensional inorganic fillers in a polymer matrix that is readily scalable to prepare high performance dielectrics for capacitors.

Conflicts of interest

There are no conflicts to declare.

Acknowledgements

The authors would like to acknowledge funding from National Natural Science Foundation of China (51672311), Hunan Natural Science Foundation (2019JJ40349), and State Key Laboratory of Powder Metallurgy, Central South University, Changsha, China.

Notes and references

1 N. Meng, X. Ren, G. Santagiuliana, L. Ventura, H. Zhang, J. Wu, H. Yan, M. J. Reece and E. Bilotti, *Nat. Commun.*, 2019, **10**, 4535.
2 R. Guo, J. I. Roscow, C. R. Bowen, H. Luo, Y. Huang, Y. Ma, K. Zhou and D. Zhang, *J. Mater. Chem. A*, 2020, **8**, 3135–3144.
3 X. Huang, B. Sun, Y. Zhu, S. Li and P. Jiang, *Prog. Mater. Sci.*, 2019, **100**, 187–225.
4 Y. Zhu, Y. Zhu, X. Huang, J. Chen, Q. Li, J. He and P. Jiang, *Adv. Energy Mater.*, 2019, **9**, 1901826.
5 Q. Li, L. Chen, M. R. Gadinski, S. Zhang, G. Zhang, H. Li, A. Haque, L.-Q. Chen, T. N. Jackson and Q. Wang, *Nature*, 2015, **523**, 576–579.
6 X. Zhang, B.-W. Li, L. Dong, H. Liu, W. Chen, Y. Shen and C.-W. Nan, *Adv. Mater. Interfaces*, 2018, **5**, 1800096.
7 Z. Pan, L. Yao, J. Zhai, X. Yao and H. Chen, *Adv. Mater.*, 2018, **30**, 1705662.
8 H. Luo, X. Zhou, C. Ellingford, Y. Zhang, S. Chen, K. Zhou, D. Zhang, C. R. Bowen and C. Wan, *Chem. Soc. Rev.*, 2019, **48**, 4424–4465.
9 A. Mannodi-Kanakkithodi, G. M. Treich, T. D. Huan, R. Ma, M. Tefferi, Y. Cao, G. A. Sotzing and R. Ramprasad, *Adv. Mater.*, 2016, **28**, 6277–6291.
10 Z. M. Dang, J. K. Yuan, S. H. Yao and R. J. Liao, *Adv. Mater.*, 2013, **25**, 6334–6365.
11 Z.-M. Dang, M.-S. Zheng and J.-W. Zha, *Small*, 2016, **12**, 1688–1701.
12 G. Wang, X. Huang and P. Jiang, *ACS Appl. Mater. Interfaces*, 2015, **7**, 18017–18027.
13 Y. Wang, L. Wang, Q. Yuan, J. Chen, Y. Niu, X. Xu, Y. Cheng, B. Yao, Q. Wang and H. Wang, *Nano Energy*, 2018, **44**, 364–370.
14 N. L. Meereboer, I. Terzic, G. Portale and K. Loos, *Nano Energy*, 2019, **64**, 103939.
15 Y. Wang, L. Wang, Q. Yuan, Y. Niu, J. Chen, Q. Wang and H. Wang, *J. Mater. Chem. A*, 2017, **5**, 10849–10855.
16 K. Bi, M. Bi, Y. Hao, W. Luo, Z. Cai, X. Wang and Y. Huang, *Nano Energy*, 2018, **51**, 513–523.
17 Z. Yao, Z. Song, H. Hao, Z. Yu, M. Cao, S. Zhang, M. T. Lanagan and H. Liu, *Adv. Mater.*, 2017, **29**, 1601727.
18 H. Tang, Y. Lin and H. A. Sodano, *Adv. Energy Mater.*, 2013, **3**, 451–456.
19 P. Kim, N. M. Doss, J. P. Tillotson, P. J. Hotchkiss, M.-J. Pan, S. R. Marder, J. Li, J. P. Calame and J. W. Perry, *ACS Nano*, 2009, **3**, 2581–2592.
20 H. Tang and H. A. Sodano, *Nano Lett.*, 2013, **13**, 1373–1379.
21 H. Tang, Y. Lin and H. A. Sodano, *Adv. Energy Mater.*, 2012, **2**, 469–476.
22 D. Zhang, C. Ma, X. Zhou, S. Chen, H. Luo, C. R. Bowen and K. Zhou, *J. Phys. Chem. C*, 2017, **121**, 20075–20083.
23 D. Zhang, X. Zhou, J. Roscow, K. Zhou, L. Wang, H. Luo and C. R. Bowen, *Sci. Rep.*, 2017, **7**, 45179.
24 H. Luo, S. Chen, L. Liu, X. Zhou, C. Ma, W. Liu and D. Zhang, *ACS Sustainable Chem. Eng.*, 2019, **7**, 3145–3153.

25 H. Luo, J. Roscow, X. Zhou, S. Chen, X. Han, K. Zhou, D. Zhang and C. R. Bowen, *J. Mater. Chem. A*, 2017, **5**, 7091–7102.
26 D. Zhang, W. Liu, R. Guo, K. Zhou and H. Luo, *Adv. Sci.*, 2018, **5**, 1700512.
27 D. Zhang, W. Liu, L. Tang, K. Zhou and H. Luo, *Appl. Phys. Lett.*, 2017, **110**, 133902.
28 H. Luo, C. Ma, X. Zhou, S. Chen and D. Zhang, *Macromolecules*, 2017, **50**, 5132–5137.
29 J. Li, P. Khanchaitit, K. Han and Q. Wang, *Chem. Mater.*, 2010, **22**, 5350–5357.
30 T. Kim, R. Trangkanukulkij and W. S. Kim, *Sci. Rep.*, 2018, **8**, 3805.
31 N. Hu, Y. Karube, C. Yan, Z. Masuda and H. Fukunaga, *Acta Mater.*, 2008, **56**, 2929–2936.
32 S.-L. Zhong, L.-J. Yin, J.-Y. Pei, X.-Y. Li, S.-J. Wang and Z.-M. Dang, *Appl. Phys. Lett.*, 2018, **113**, 122904.
33 C. Andrews, Y. Lin and H. A. Sodano, *Smart Mater. Struct.*, 2010, **19**, 025018.
34 B. Xie, H. Zhang, Q. Zhang, J. Zang, C. Yang, Q. Wang, M.-Y. Li and S. Jiang, *J. Mater. Chem. A*, 2017, **5**, 6070–6078.
35 X. Zhang, J. Jiang, Z. Shen, Z. Dan, M. Li, Y. Lin, C.-W. Nan, L. Chen and Y. Shen, *Adv. Mater.*, 2018, **30**, 1707269.
36 D. He, Y. Wang, S. Song, S. Liu and Y. Deng, *ACS Appl. Mater. Interfaces*, 2017, **9**, 44839–44846.
37 M. Gao, L. Li, W. Li, H. Zhou and Y. Song, *Adv. Sci.*, 2016, **3**, 1600120.
38 J. H. Kim, S. Lee, M. Wajahat, H. Jeong, W. S. Chang, H. J. Jeong, J. R. Yang, J. T. Kim and S. K. Seol, *ACS Nano*, 2016, **10**, 8879.
39 B. G. Compton and J. A. Lewis, *Adv. Mater.*, 2015, **26**, 5930–5935.
40 D. E. Yunus, W. Shi, S. Sohrabi and Y. Liu, *Nanotechnology*, 2016, **27**, 495302.
41 N. Phatharapeetranun, B. Ksapabutr, D. Marani, J. R. Bowen and V. Esposito, *J. Mater. Chem. C*, 2017, **5**, 12430–12440.
42 K. Kanguk, Z. Wei, Q. Xin, A. Chase, W. R. Mccall, C. Shaochen and D. J. Sirbuly, *ACS Nano*, 2014, **8**, 9799.
43 B. Xie, Q. Zhang, H. Zhang, G. Zhang, S. Qiu and S. Jiang, *Ceram. Int.*, 2016, **42**, 19012–19018.
44 J. Liao, H. Chen, L. Hang, X. Wang, K. Zhou and Z. Dou, *J. Mater. Chem. C*, 2017, **5**, 5867–5871.
45 B. Jiang, J. Iocozzia, L. Zhao, H. Zhang, Y.-W. Harn, Y. Chen and Z. Lin, *Chem. Soc. Rev.*, 2019, **48**, 1194–1228.
46 W. Xu, G. Yang, L. Jin, J. Liu, Y. Zhang, Z. Zhang and Z. Jiang, *ACS Appl. Mater. Interfaces*, 2018, **10**, 11233–11241.
47 P. Hu, S. Gao, Y. Zhang, L. Zhang and C. Wang, *Compos. Sci. Technol.*, 2018, **156**, 109–116.
48 Y. N. Hao, X. H. Wang, S. O'Brien, J. Lombardi and L. T. Li, *J. Mater. Chem. C*, 2015, **3**, 9740–9747.
49 N. Phatharapeetranun, B. Ksapabutr, D. Marani, J. R. Bowen and V. Esposito, *J. Mater. Chem. C*, 2017, **5**, 12430–12440.
50 M. Gao, L. Li, W. Li, H. Zhou and Y. Song, *Adv. Sci.*, 2016, **3**, 1600120.
51 Y. P. Ma, H. Luo, X. F. Zhou, R. Guo, F. Dang, K. C. Zhou and D. Zhang, *Nanoscale*, 2020, DOI: 10.1039/C9NR08572F.
52 H. Luo, D. Zhang, C. Jiang, X. Yuan, C. Chen and K. Zhou, *ACS Appl. Mater. Interfaces*, 2015, **7**, 8061–8069.